THERMO-HYDRAULIC ANALYSIS OF STRUCTURED HEAT TRANSFER SURFACES UNDER CONSIDERATION OF PARTICULATE FOULING USING A MULTIPHASE EULERIAN-LAGRANGIAN METHOD

R. Kasper[1], J. Turnow[1] and N. Kornev[1]

[1]Chair of Modeling and Simulation (LeMoS), University of Rostock,
Albert-Einstein-Str. 2, 18059 Rostock, Germany (robert.kasper@uni-rostock.de)

ABSTRACT

A novel multiphase method for the numerical simulation of particulate fouling of structured heat transfer surfaces is introduced. The proposed method is based on a coupling of the Lagrangian-Particle-Tracking (LPT) and Eulerian approach. Therefore, suspended particles are simulated according to their natural behavior by means of LPT as solid spherical particles whereas the carrier phase is simulated using the Eulerian approach. Large Eddy Simulations (LES) are performed for fully developed turbulent channel flows at $\mathrm{Re}_\tau = 395$ with selected structured surfaces (square cavity and spherical dimple) and foulant particle mass loading ratios up to $\beta = \dot{m}_p/\dot{m}_f = 2 \times 10^{-3}$ using a dynamic one equation eddy-viscosity turbulence model. These simulations demonstrate the great capabilities of the proposed method and reveal a slightly better fouling performance and thermo-hydraulic efficiency of the spherical dimple compared to the square cavity.

INTRODUCTION

Particulate fouling of heat transfer surfaces due to suspended material within the heat exchanger working fluid is still one of the most important problems in heat exchangers. It has been described as the major unresolved and most challenging problem in heat transfer (Awad, 2011). Fouling increases the heat transfer resistance and reduces the effectiveness of heat exchangers which causes higher fuel consumption, maintenance costs and costs due to production loss (Müller-Steinhagen, 2010). Despite the fact that particulate fouling reduces the heat transfer and increases the pressure loss, the performance of heat transfer enhancement methods like ribs, fins or dimples is commonly characterized by the thermo-hydraulic efficiency (Gee and Webb, 1980) or number of transfer units NTU (Shah and Sekulić, 2003), which does not include any information about the fouling behavior. In addition to it, a more or less universal method for the prediction of particulate fouling does still not exist. Existing fouling models (e.g., Kern and Seaton (1969) and Taborek et al. (1972)) are derived for numerous assumptions and simplifications. Hence, existing fouling modeling approaches are unsuitable for a general prediction of particulate fouling and a detailed analysis of fundamental fouling mechanisms. Due to the steadily growing computational resources, the simulation of highly complex processes like particulate fouling using computational fluid dynamics (CFD) becomes more and more important and could be a reliable alternative to expensive experimental measurements. In contrast to several numerical investigations of heat transfer enhancement methods, e.g. Elyyan et al. (2008) and Turnow et al. (2011), CFD studies of structured heat transfer surfaces considering particulate fouling are relatively seldom. Moreover, a extensive analysis of the interaction between local flow structures and fouling deposits using transient, large-scale resolving numerical methods such as LES or hybrid URANS-LES does not exist at this moment.

The present study is aimed to fill up this lack of knowledge by introducing a new multiphase Eulerian-Lagrangian approach which is suitable for CFD studies of heat transfer enhancement methods under consideration of particulate fouling using large-scale resolving methods. This provides the opportunity to analyze the interaction between local flow structures and different fouling processes in a more comprehensive way.

NUMERICAL METHODS

The numerical simulation of particulate fouling on heat transfer surfaces is complex and it consists mainly of the deposition of small suspended particles due to adhesion and sedimentation of larger particles onto horizontal surfaces resulting from gravitational forces. Therefore, the proposed multiphase method is composed of two different branches which are closely related to each other. The first one is the Lagrangian branch and describes the physics of the suspended particles or respectively the foulant using the LPT. This branch is mainly responsible for the mass transport of the particles to the heat transfer surfaces, the formation of fouling deposits due to adhesion and sedimentation and also the removal of fouling deposits due to local shear forces. The second one is the Eulerian branch which determines the flow fields of the carrier flow with respect to the fouling deposits.

Lagrangian branch

The description of isothermal particle motions within a fluid using the Lagrangian-Particle-Tracking (LPT) requires

ISBN: 978-0-9984188-0-3; Published online www.heatexchanger-fouling.com

the solution of the following set of ordinary differential equations, to calculate the particle location and the linear as well as the angular particle velocity at any time:

$$\frac{\mathrm{d}\mathbf{x}_p}{\mathrm{d}t} = \mathbf{u}_p, \tag{1}$$

$$m_p \frac{\mathrm{d}\mathbf{u}_p}{\mathrm{d}t} = \sum \mathbf{F}_i, \tag{2}$$

$$I_p \frac{\mathrm{d}\omega_p}{\mathrm{d}t} = \sum \mathbf{T}, \tag{3}$$

where m_p is the particle mass, I_p is the moment of inertia, $\mathbf{F}_i$ includes all forces acting on the particle and $\mathbf{T}$ is the torque acting on the rotating particle due to viscous interaction with the carrier fluid (Sommerfeld, 2010). Newton's second law of motion, Eq. (2), requires the consideration of all relevant forces acting (e.g. drag, gravity and pressure forces) on the particle:

$$m_p \frac{\mathrm{d}\mathbf{u}_p}{\mathrm{d}t} = \sum \mathbf{F}_i = \mathbf{F_D} + \mathbf{F_G} + \mathbf{F_P} + ... \tag{4}$$

However, analytical representation for different forces exists only for small particle Reynolds numbers respectively for the Stokes regime (Crow et al., 2011). Thus, the drag force is expressed more generally in terms of a drag coefficient C_D. The implemented drag model is based on the particle Reynolds number, which is defined as

$$\mathrm{Re}_p = \frac{\rho_f D_p \left|\mathbf{u}_f - \mathbf{u}_p\right|}{\mu_f}, \tag{5}$$

with the density ρ_f and the dynamic viscosity μ_f of the fluid or continuous phase, the particle diameter D_p and the magnitude of the relative slip velocity $\left|\mathbf{u}_f - \mathbf{u}_p\right|$. The drag coefficient is determined using the following drag model based on the correlation proposed by Putnam (1961):

$$C_D = \begin{cases} \frac{24}{\mathrm{Re}_p}\left(1 + \frac{1}{6}\mathrm{Re}_p^{2/3}\right) & \text{if } \mathrm{Re}_p \leq 1000 \\ 0.424 & \text{if } \mathrm{Re}_p > 1000, \end{cases} \tag{6}$$

which is suitable to higher Reynolds numbers ($\mathrm{Re}_p < 1000$) and ensures the correct limiting behavior within the Newton regime. After determination of the drag coefficient, the basic force representation is used to evaluate the drag force for a spherical particle:

$$\mathbf{F_D} = C_D \frac{\pi D_p^2}{8} \rho_f \left(\mathbf{u}_f - \mathbf{u}_p\right) \left|\mathbf{u}_f - \mathbf{u}_p\right|. \tag{7}$$

In addition to the drag force, the gravitational and buoyancy force and the pressure gradient force has to be taken into account as well. Within the used LPT, gravitation and buoyancy is computed as follows as one total force

$$\mathbf{F_G} = m_p \mathbf{g} \left(1 - \frac{\rho_f}{\rho_p}\right), \tag{8}$$

where $\mathbf{g}$ is the gravitational acceleration vector. The resultant force due to a local fluid pressure gradient acting on a particle can be defined as

$$\mathbf{F_P} = -\frac{\pi D_p^3}{6} \nabla p. \tag{9}$$

Expressing the pressure gradient ∇p in terms of the differential form of the momentum equation, the force due to a local pressure gradient can be evaluated by

$$\mathbf{F_P} = \rho_f \frac{\pi D_p^3}{6} \left(\frac{\mathrm{D}\mathbf{u}_f}{\mathrm{D}t} - \nabla \cdot \nu_f \left(\nabla \mathbf{u}_f + \nabla \mathbf{u}_f^T\right) \right). \tag{10}$$

From Eq. (10) it is evident that the pressure gradient force is proportional to the displaced fluid mass. Therefore, this force may be neglected in gas-solid flows and is of importance only in liquid-solid flows (Sommerfeld, 2010).

The acceleration or deceleration of a particle in a fluid will also require the acceleration or deceleration of a certain amount of the fluid surrounding this particle (according to Newton's third law). This additional force is known as added mass force or sometimes referred to as virtual mass force and is modeled as an increase of the particles effective mass:

$$m_A = m_p \frac{\rho_f}{\rho_p} C_A, \tag{11}$$

where C_A is the so-called added mass coefficient. This coefficient can be exactly derived for spherical particles from potential theory and is $C_A = 1/2$, which is also a relatively accurate approximation for viscous flows, especially in case of a small velocity difference between fluid and particle (Crow et al., 2011). Finally the added mass force is expressed as:

$$\mathbf{F_A} = C_A \rho_f \frac{\pi D_p^3}{6} \left(\frac{\mathrm{D}\mathbf{u}_f}{\mathrm{D}t} - \frac{\mathrm{d}\mathbf{u}_p}{\mathrm{d}t} \right). \tag{12}$$

Furthermore, in case of particulate fouling the consideration of thermophoresis could be extremely important (this applies especially to gases as for liquids), whereby a 'thermal' force moves fine particles in the direction of negative temperature gradients (Epstein, 1988). Hence, hot walls prevents and cold walls promotes particle depositions. The thermophoretic force is considered as:

$$\mathbf{F_T} = -D_{T,p} \frac{\nabla T}{T}, \tag{13}$$

where $D_{T,p}$ is the thermophoretic coefficient, which can be derived as suggested by Talbot et al. (1979).

The last force considered within this work arises due to local shear flows and therefore from a non-uniform velocity distribution over the particle surface. This lift force is called Saffman force and is modeled using the Saffman-Mei model, derived by Saffman (1965, 1968) and advanced by Mei (1992). In order to determine the lift force due to local shear flows, the shear Reynolds number has to be calculated:

$$\mathrm{Re}_s = \frac{\rho_f D_p^2 \left|\nabla \times \mathbf{u}_f\right|}{\mu_f}, \tag{14}$$

which is used to evaluate the coefficients of the Saffman-Mei

ISBN: 978-0-9984188-0-3; Published online www.heatexchanger-fouling.com

model:

$$\beta = \frac{1}{2}\frac{\mathrm{Re}_s}{\mathrm{Re}_p}, \qquad \alpha = 0.3314\sqrt{\beta},$$
$$f = (1-\alpha)\exp(-0.1\mathrm{Re}_p) + \alpha. \tag{15}$$

Afterwards the lift coefficient C_{LS} is calculated using the following approximation:

$$C_{LS} = \begin{cases} 6.46f & \text{if } \mathrm{Re}_p < 40 \\ 6.46 \cdot 0.0524\sqrt{\beta \mathrm{Re}_p} & \text{if } \mathrm{Re}_p \geq 40. \end{cases} \tag{16}$$

The lift coefficient C_{LS} is now expressed in terms of a non-dimensional lift coefficient

$$C_L = \frac{3}{2\pi\sqrt{\mathrm{Re}_s}} C_{LS}. \tag{17}$$

This conversion allows a more universal way to determine the lift force using any conceivable force model. Finally the lift force is calculated as:

$$\mathbf{F_L} = C_L \rho_f \frac{\pi D_p^3}{6} \left(\mathbf{u}_f - \mathbf{u}_p\right) \times \left(\nabla \times \mathbf{u}_f\right). \tag{18}$$

In summary, it can be stated that the proposed LPT is capable to consider the most important forces acting on a particle. Because numerical simulations of Sommerfeld have shown that the consideration of the Basset force increases the computational time by a factor of about 10 (Sommerfeld, 2010), this force is neglected. This strategy is valid for small density ratios $\rho_f/\rho_p << 1$ (Crow et al., 2011), which is not the case for liquid-solid flows as investigated below. Thus, the influence of the Basset force has to be analyzed in the future.
However, another important concept in the analysis of dispersed multiphase flows is phase coupling. One-way coupling exists if the carrier flow effects the particles while there is no reverse effect. If there is a mutual effect between carrier flow and particles, then the flow is two-way coupled. In case of dense flows, there will be an additional interaction between the particles itself, which is meant by four-way coupling (Elghobashi, 1994). The proposed method is generally capable to consider all types of phase coupling using a time-dependent volumetric source term within the momentum balance of the carrier fluid and a soft-sphere model (including a spring, slider and dash-pot) for the particle-particle interactions.

Formation of fouling deposits

The physical modeling of the deposition of the foulant on heat transfer surfaces is very crucial. Due to the fact that particle deposition is mainly caused by particle-wall adhesion within this work (this assumption is applicable to particle diameters of $D_p \leq 100\,\mu\mathrm{m}$ (Epstein, 1988)), the implemented model is based on the suggestions of Löffler and Muhr (1972) and furthermore Heinl and Bohnet (2005). This model consists of an energy balance around the particle-wall and particle-fouling collision. Thus, a critical particle velocity can be derived according to the DLVO theory from a local energy balance which contains the kinetic energy before and after the collision, the energy ratio describing the adhesion due to London-Van der Waals forces and a specific amount considering the energy loss of a particle due to particle-wall and particle-fouling collision. From the condition of adhesion (i.e., a particle is not able release from the wall after the collision), the critical particle velocity yields:

$$u_{p,crit} = \sqrt{\left(\frac{\hbar\varpi}{eD_p 4\pi^2 z_0^2}\right)^2 \frac{3}{4H\rho_p}}, \tag{19}$$

where $\hbar\varpi$ is the Lifshitz-Van der Waals energy, z_0 is the distance at contact, H is the strength of the contact wall and e is the coefficient of restitution. It should be mentioned at this point, that the determination of the critical particle velocity Eq. (19) can be easily extended for the consideration of electrostatic double-layer interaction forces (Heinl, 2005). However, only London-Van der Waals forces are considered in a first step. Thus, the condition of sticking is achieved, if the particle velocity before the wall collision (impact velocity) is smaller then the critical particle velocity:

$$\left|\mathbf{u}_p\right| \leq u_{p,crit}. \tag{20}$$

To increase the computational efficiency of our approach, particles which fulfills the adhesion condition, Eq. (20), are converted into an additional solid phase (fouling deposits) and will be deactivated within the LPT. Thus, the amount of particles is kept nearly constant during the calculations which reduces the computational time enormously. The initiated fouling volume or fouling phase fraction α is evaluated by the particle volume with respect to the cell volume:

$$\alpha_{new,i} = \alpha_{old,i} + \frac{V_p}{V_{c,i}}, \tag{21}$$

where $\alpha_{old,i}$ is the phase fraction from the previous time step, V_p and $V_{c,i}$ are the particle and cell volume respectively. Fig. 1 shows the basic concept of the implemented phase conversion algorithm.

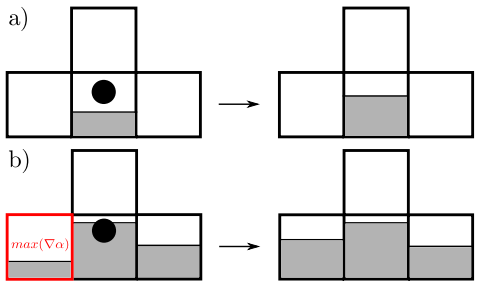

Fig. 1. Basic mechanism of the phase conversion algorithm: a) $V_c > V_p$ and b) $V_c < V_p$

According to this, it can be distinguished between two different cases if a deposited particle has to be converted into the fouling phase. If the residual local cell volume is greater than the particle volume, the new phase fraction α can be simply determined using Eq. (21). If the remaining local cell volume is smaller than the particle volume, the phase fraction is allocated to the neighbor cell with the maximum cell-based

phase fraction gradient $\max(\nabla\alpha)$. Hence the neighbor cell with the lowest phase fraction is filled with the fouling phase. To consider the influence of the fouling phase, an additional porosity source term (based on Darcy's law)

$$\mathbf{S}_p = \alpha \frac{\mu_f}{K} \mathbf{u}_f, \tag{22}$$

has been introduced into the momentum balance equation, where K is the isotropic permeability of the fouling phase. Thus, the blocking effect or flow section contraction due to deposited particles is not explicitly considered within the calculations but rather is modeled implicitly in terms of a porous fouling layer. Furthermore any physical property φ_i (e.g., density, dynamic/kinematic viscosity or thermal diffusivity) for partially filled cells is interpolated as follows:

$$\varphi_i = \alpha \cdot \varphi_{fouling} + (1-\alpha) \cdot \varphi_{fluid}, \tag{23}$$

whereas the physical properties of the carrier fluid are fully applied at cells without fouling phase ($\alpha = 0$) and cells which are completely occupied by the fouling phase ($\alpha = 1$) takes the physical properties of the fouling material. This procedure allows likewise the evaluation of the heat transfer under consideration of particulate fouling and prevents the solving of an additional advection/transport equation for the fouling phase and furthermore the application of costly re-meshing procedures.

Removal of fouling deposits

The removal or re-entrainment process of fouling deposits due to high local shear forces is an important mechanism, which has to be considered for a physical simulation of the fouling behavior. Therefore, a removal model is derived based on the suggestions of Kern and Seaton (1969) and Taborek et al. (1972):

$$\alpha_{removed} = \min\left(\frac{|\tau_c|}{\tau_{rel}} \frac{V_p}{V_c}, \frac{V_p}{V_c}\right), \tag{24}$$

where τ_{rel} is a relative shear stress and τ_c is the local cell-based shear stress. The relative shear stress has to be measured in experiments and can be interpreted as a strength threshold value at which the removal and re-entrainment of fouling deposits within each individual grid cell starts. The number of spherical particles for the re-entrainment into the carrier fluid can be determined using the definition of the sphere volume:

$$n = \frac{\alpha_{removed} V_c}{\pi D_p^3/6}. \tag{25}$$

The removed fouling particles will be reactivated and become part of the LPT again, whereby the initial momentum and forces are calculated according to the force models described above.

Eulerian branch

The continuous phase or carrier fluid is assumed to be incompressible. Therefore, the governing equations are the incompressible Navier-Stokes equations (extended by the porosity source term $\mathbf{S}_p$, which takes the influence of the fouling layer into account), the continuity equation and a passive scalar transport equation for the temperature. This system of partial differential equations is solved numerically using a 3-D finite volume method. Although the turbulence modeling is generic Large Eddy Simulations (LES) are carried out to investigate the interaction between local vortex structures and particulate fouling. LES is a widely used technique for simulating turbulent flows and allows one to explicitly solve for the large eddies and implicitly account for the small eddies by using a subgrid-scale model (SGS model).

Large Eddy Simulation (LES)

The LES equations are derived by filtering the continuity equation, the Navier-Stokes equations and the simplified energy balance equation using an implicit box-filter with filter width $\overline{\Delta}$:

$$\nabla \cdot \overline{\mathbf{u}} = 0, \tag{26}$$

$$\frac{\partial \overline{\mathbf{u}}}{\partial t} + \nabla \cdot (\overline{\mathbf{u}}\,\overline{\mathbf{u}}) = -\frac{1}{\rho}\nabla p + \nabla \cdot \nu \left(\nabla \overline{\mathbf{u}} + \nabla \overline{\mathbf{u}}^T\right) - \nabla \cdot \tau_{SGS} - \overline{\mathbf{S}}_p, \tag{27}$$

$$\frac{\partial \overline{T}}{\partial t} + \nabla \cdot \left(\overline{\mathbf{u}}\,\overline{T}\right) = \nabla \cdot \left(a(\alpha)\nabla \overline{T}\right) - \nabla \cdot \mathbf{J}_{SGS}. \tag{28}$$

The unclosed subgrid-scale stress tensor $\tau_{SGS} = \overline{\mathbf{u}\mathbf{u}} - \overline{\mathbf{u}}\,\overline{\mathbf{u}}$ is modeled using a dynamic one equation eddy-viscosity model proposed by Yoshizawa and Horiuti (1985) and Kim and Menon (1995):

$$\frac{\partial k_{SGS}}{\partial t} + \nabla \cdot (k_{SGS}\overline{\mathbf{u}}) = \nabla \cdot \left[(\nu + \nu_{SGS})\nabla k_{SGS}\right] - \tau_{SGS} : \overline{\mathbf{S}} - C_\varepsilon \frac{k_{SGS}^{3/2}}{\overline{\Delta}}, \tag{29}$$

where the subgrid-scale eddy-viscosity ν_{SGS} and the subgrid-scale stress tensor τ_{SGS} can be found from

$$\nu_{SGS} = C_k \overline{\Delta} k_{SGS}^{1/2}, \tag{30}$$

$$\tau_{SGS} = -2\nu_{SGS}\overline{\mathbf{S}} + \frac{2}{3} k_{SGS} \mathbf{I}. \tag{31}$$

This SGS model uses the modeled balance Eq. (29) to simulate the behavior of the subgrid-scale kinetic energy k_{SGS} in which the dynamic procedure of Germano et al. (1991) is applied to evaluate all required coefficients dynamically in space and time. The subgrid-scale heat flux $\mathbf{J}_{SGS}$ is considered using a gradient-diffusion approach.

RESULTS

Computational setup

Two academical test cases, a smooth narrow channel with a spherical dimple and a square cavity, have been chosen to investigate the fouling behavior of structured heat transfer surfaces by our proposed approach. The computational domain for both test cases is shown in Fig. 2. The origin of the coordinate system is located in the center of the dimple respectively

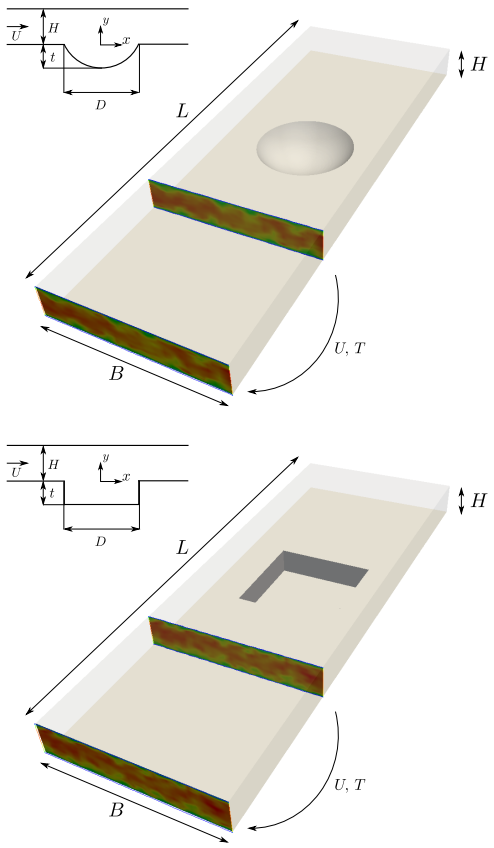

Fig. 2. Computational domain for a smooth channel with a single spherical dimple (above) and a square cavity (below)

the cavity and is projected onto the lower wall plane, therefore the lower wall is located at $y/H = 0.0$. The length of the channel is $L = 0.23\,\mathrm{m}$, while channel height H and channel width B is set to $H = 0.015\,\mathrm{m}$ and $B = 0.08\,\mathrm{m}$. For the spherical dimple with a sharp edge a diameter of $D = 0.046\,\mathrm{m}$ and a dimple depth $t = 0.012\,\mathrm{m}$ is chosen, while the side length of the square cavity equals the dimple diameter D and the cavity depth is likewise set to $t = 0.012\,\mathrm{m}$. Periodic boundary conditions were applied in spanwise direction, whereas no slip boundary conditions were set at the lower and upper channel walls. Turbulent inlet conditions were produced using a recycling method, which copies the turbulent velocity and temperature field from a plane downstream the channel entrance back onto the inlet. The non-dimensional form of the temperature

$$T^+ = \frac{T - T_\infty}{T_w - T_\infty} \tag{32}$$

is used, where a constant $T^+ = 1$ is assumed at the lower wall. The molecular Prandtl number Pr was set to 0.71 in all simulations, whereas the turbulent Prandtl number Pr_t is 0.9. The Reynolds number based on the averaged bulk velocity u_b and the dimple diameter or respectively the cavity side length D was equal to $\mathrm{Re}_D = 42{,}000$. To assure grid independence of the obtained results a series of calculations on different grid resolutions was carried out. Therefore block structured curvilinear grids consisting of around 7.8×10^5, 1.6×10^6 and 3.3×10^6 cells was used. In spanwise and streamwise direction an equidistant grad spacing is applied, whereas in wall-normal direction a homogeneous grid stretching is used to place the first grid node inside of the laminar sublayer at $y^+ \approx 1$. Spherical monodisperse silicon dioxide particles (SiO_2) are randomly injected within the flow inlet during all fouling simulations. The physical properties of the these foulant particles are given in Tab. 1. Based on earlier experimental fouling investigations on heat exchangers by Blöchl and Müller-Steinhagen (1990) a particle mass loading ratio of $\beta = \dot{m}_p/\dot{m}_f = 10^{-3}$ and $\beta = 2 \times 10^{-3}$ is chosen to ensure an asymptotic fouling layer growth and a steady-state within a few minutes of physical real time. The estimated volume fraction of the dispersed phase is $\alpha_d < 0.001$ which corresponds to a dilute flow and allows the negligence of particle collisions (Crow et al., 2011). Hence, only two-way coupling is considered during the simulations by applying a time-dependent volumetric source term to the momentum balance equation.

Tab. 1. Thermo-physical properties of the injected foulant particles

Diameter	$D_p = 20\,\mu\mathrm{m}$
Density	$\rho_p = 2500\,\mathrm{kg/m^3}$
Thermal conductivity	$k_p = 1.4\,\mathrm{W/(mK)}$
Specific heat capacity	$c_p = 1.052\,\mathrm{kJ/(kgK)}$

Fully developed turbulent flow in a plane channel with a single spherical dimple

Numerical results for a smooth channel in combination with a single spherical dimple are validated using the experimental data published by Terekhov et al. (1997) and Turnow et al. (2011). Fig. 3 shows the profile of the normalized streamwise velocity $\langle u \rangle / u_0$ and Reynolds stress $\langle u_{rms} \rangle / u_0$ in flow direction received from URANS (k-ω-SST model with fine grid; only for comparative purposes) and LES for three different grid resolutions and from Laser Doppler Anemometry (LDA) measurements along the y-axis at $x/D = 0.0$ and $z/H = 0.0$ (center of the dimple). The numerical results are obtained for Reynolds number $\mathrm{Re}_D = 42{,}000$ and are normalized by the maximum velocity u_0 in the center of the channel at $y = H/2$. A satisfactory overall agreement of calculated and measured mean velocity profiles has been obtained for all three grid resolutions and streamwise locations x/D. The mean velocity profiles from LES and URANS matches well with the measurements in the center of the channel where the maximum flow velocity occurs and even in the upper near wall region. However, slight deviations from the measured profiles can be registered for both methods and all grid resolutions inside of the spherical dimple within the distinct recirculation zone. Nevertheless, since URANS and LES results are in good agreement in this region, the likeliest reason for the discrepancy between measurements and calculations might be LDA measurement problems in close proximity of the wall (Turnow, 2011). From the mean velocity profiles one can observe, that the strongest velocity gradients arises at the level

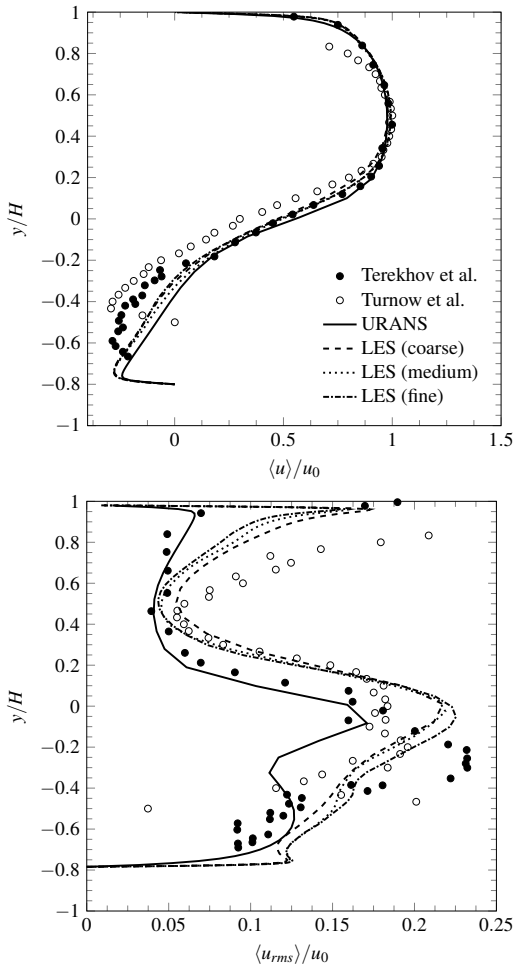

Fig. 3. Normalized, time-averaged streamwise velocity and Reynolds stress profiles at $x/D = 0.0$ and $z/D = 0.0$ obtained from URANS and LES in comparison with experiments of Terekhov et al. (1997) and Turnow et al. (2011)

of lower channel wall ($y/H = 0.0$). The instabilities of the shear layer within this region results into strong vortices and therefore in high Reynolds stresses, which can be observed in all Reynolds stress profiles. Unlike the mean velocity profiles the level of the Reynolds stresses and furthermore the location of the maximum turbulent fluctuations measured in experiments can only be gained using LES. A deviation between the measured and calculated location of the maximum Reynolds stresses are notable within the center of the dimple at position $x/D = 0.0$. The weakness of URANS is clearly visible in the near wall region and the level of the lower wall, where the magnitude of the turbulent fluctuations can not be captured. Due to the great importance of capturing the Reynolds stresses or fluid shear forces in order to calculate a the removal rate of deposited particles, URANS seems to be inappropriate for further investigations.

Probably the most important feature of the investigated spherical dimple with a dimple depth to dimple diameter ratio of $t/D = 0.26$ can be observed from the phase-averaged streamline pattern given in Fig. 4. The streamlines shows unsteady asymmetrical vortex structures inside the dimple, which alter their orientation arbitrary from $-45°$ to $+45°$ with respect to the main flow direction. The existence of long period self-sustained oscillations within the dimple flow could be investigated and approved as well experimentally (Terekhov, 1997) as numerically using highly resolved LES (Turnow, 2011) for dimple depth to dimple diameter ratios of $t/D = 0.26$ and larger. In contrast to experimental observations and LES results the asymmetric vortex structures obtained from URANS are steady and predicts only one of the two extreme vortex positions ($\pm 45°$) in time-averaged flow pattern which are switching in reality nearly periodically. It is assumed that the self-sustained oscillations and periodically outburst due to unsteady asymmetric vortex structures enhance the wall shear stress and therefore promotes a possible self-cleaning process inside the spherical dimple and at the lower channel wall. Thus, LES is chosen to simulate the particulate fouling and to investigate its influence on the integral heat transfer and pressure loss.

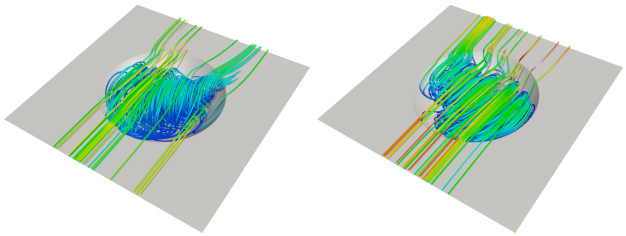

Fig. 4. Different orientations ($\pm 45°$) of the oscillating vortex structures inside the spherical dimple for $\mathrm{Re}_D = 42{,}000$

PARTICULATE FOULING OF STRUCTURED HEAT TRANSFER SURFACES

To investigate the influence of particulate fouling on the friction/pressure loss and heat transfer a series of LES using mass loading ratios up to $\beta = \dot{m}_p/\dot{m}_f = 2 \times 10^{-3}$ are carried out for a single spherical dimple and a single square cavity. Due to the results given in Fig. 3, a medium grid resolutions with around 1.6×10^6 cells seems to be sufficient to capture as well the streamwise velocity profiles as the Reynolds stresses and is chosen for the simulation of particulate fouling. The pressure loss can be expressed in terms of the Darcy friction factor

$$f = -\frac{(dp/dx)D_h}{\rho_f u_b^2/2}, \tag{33}$$

which is directly related to the Fanning friction factor by $C_f = f/4$. (dp/dx) represents the pressure gradient in streamwise direction, D_h is the hydraulic diameter of the channel, ρ_f and u_b are the density and the bulk velocity of the fluid. The heat transfer is evaluated using the Nusselt number (which relates the total heat transfer to the conductive heat transfer)

$$\mathrm{Nu} = \frac{hL}{k}, \tag{34}$$

where h is the convective heat transfer coefficient, L is a characteristic length (L is set to $2H$ due to periodic boundary

conditions in streamwise direction) and k is the thermal conductivity of the fluid. The friction coefficient f_0 and Nusselt number Nu_0 of the smooth channel are determined using the correlations of Petukhov and Gnielinski (Bejan and Kraus, 2003):

$$f_0 = \left(0.79 \ln\left(\mathrm{Re}_D\right) - 1.64\right)^{-2}, \tag{35}$$

$$\mathrm{Nu}_0 = \frac{\left(f_0/8\right)\left(\mathrm{Re}_D - 1000\right)\mathrm{Pr}}{1 + 12.7\left(f_0/8\right)^{1/2}\left(\mathrm{Pr}^{2/3} - 1\right)}. \tag{36}$$

These correlations are in terms of Reynolds number based on the pipe diameter D $\left(0.5 \leq \mathrm{Pr} \leq 2000,\ 3000 \leq \mathrm{Re}_D < 5 \times 10^6\right)$. Thus, Re_D has to be replaced by the Reynolds number based on the hydraulic diameter $D_h = 2H$ for a smooth infinitely wide channel. The time-averaged pressure loss, integral convective heat transfer (integrated using the wall surface area from $x/D = -0.75$ to $x/D = 1.75$) and thermo-hydraulic efficiency for the clean structured surfaces with respect to the smooth channel are summarized and compared in Tab. 2. The

Tab. 2. Thermo-hydraulic efficiency for different (clean) structured surfaces at $\mathrm{Re}_D = 42{,}000$

	C_f/C_{f0}	$\mathrm{Nu}/\mathrm{Nu}_0$	$\frac{(\mathrm{Nu}/\mathrm{Nu}_0)}{(C_f/C_{f0})}$	$\frac{(\mathrm{Nu}/\mathrm{Nu}_0)}{(C_f/C_{f0})^{1/3}}$
Cavity	1.600	1.292	0.808	1.105
Dimple	1.079	1.508	1.398	1.470

evaluation of both types of structured surfaces discloses the disadvantages of the square cavity due to the significant increase of pressure loss by approx. 60%, which can not be compensated by the slightly enhanced heat transfer of around 29%. Therefore, the thermo-hydraulic efficiency ranges between 0.808 and 1.105, depending on the applied definition. A quite contrary thermo-hydraulic efficiency can be achieved in case of the spherical dimple, which lies between 1.398 and 1.470. The reason for that impressive outcome is the moderate increase of pressure loss by almost 8%, which agrees with published results by Turnow et al. (2011), in comparison to the noticeable heat transfer augmentation of about 50%. Fig. 5 decipts the time-averaged Nusselt number distribution at the clean lower channel wall with both structured surfaces, where regions of high convective heat transfer rates due to large velocity magnitudes and local vortex structures are primarily obtained within the surface structures and the downstream area behind the trailing edges. Especially the spherical dimple exhibits high Nusselt numbers of 100 and more over a relatively wide area, which explains the superior heat transfer enhancement compared to the square cavity.

The analysis of the thermo-hydraulic efficiency under consideration of foulant particle mass loading ratios up to $\beta = 2 \times 10^{-3}$ are given in Tab. 3, which are less unambiguous as for the clean surfaces. The reason for this is the relatively small change of pressure loss and convective heat transfer, caused by the thin settled fouling layers after 120 s of physical real time. Nevertheless, the present results provides a first trend concerning the fouling behavior of the investigated structured surfaces. According to this the square cavity seems

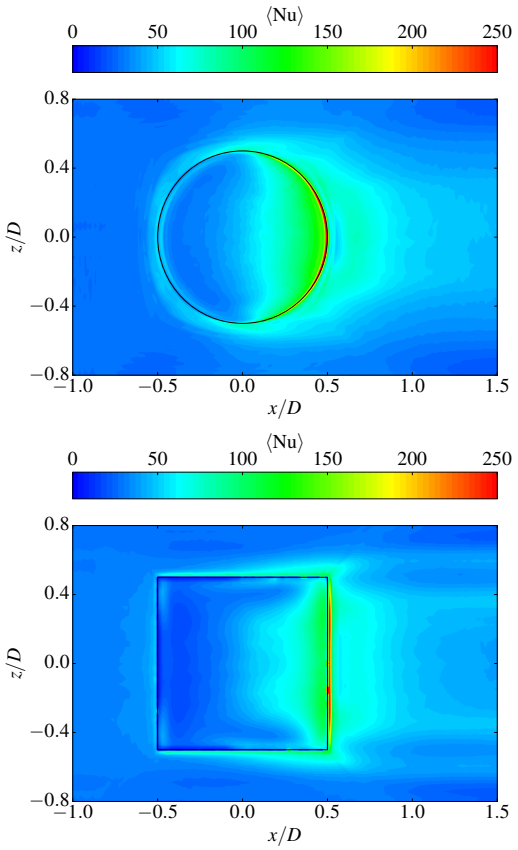

Fig. 5. Time-averaged Nusselt number distribution at the clean lower channel wall for a spherical dimple (above) and a square cavity (below) at $\mathrm{Re}_D = 42{,}000$

to be more susceptible for fouling deposits, which leads to an increase of pressure loss of approx. 2% and a reduced heat transfer by almost 0.5%. The spherical dimple shows only slightly changes in pressure loss and an almost stable convective heat transfer for all considered particle mass loading ratios β, which underlines the better fouling behavior in contrast to the cavity. Finally, Fig. 6 illustrates the distribution

Tab. 3. Thermo-hydraulic efficiency for different structured surfaces and mass loading ratios β after 120 s at $\mathrm{Re}_D = 42{,}000$

	β	C_f/C_{f0}	$\mathrm{Nu}/\mathrm{Nu}_0$	$\frac{(\mathrm{Nu}/\mathrm{Nu}_0)}{(C_f/C_{f0})^{1/3}}$
Cavity	10^{-3}	1.621	1.287	1.100
Dimple	10^{-3}	1.075	1.505	1.469
Cavity	2×10^{-3}	1.622	1.290	1.098
Dimple	2×10^{-3}	1.083	1.508	1.468

and thickness x_f of the settled fouling layer for both structured surfaces after 120 s of simulated physical real time for an foulant particle mass ratio of $\beta = 2 \times 10^{-3}$. A relatively high amount of deposits with a total fouling layer height in the range of 20 μm and 100 μm can be observed within the recirculation zone of the spherical dimple in the vicinity of the leading edge, whereas no fouling is detected in the lee side

of the dimple where the reattachment point of the flow lies. Additionally, comparable less fouling deposits are obtained at the channel wall downstream of the dimple trailing edge. The reason for this observation is probably the high wall shear stress in this particular regions due to the switching asymmetric vortex structures and vortex outbursts, because both extreme positions of the alternating vortex structures ($\pm 45°$) becomes faintly visible in the fouling distribution. Moreover, due to the flow acceleration in front of the dimple no fouling occurs in the area of the dimple front edge. In case of the square cavity, highest fouling deposition rates are obtained inside the forward half of the cavity, whereas the clean area downstream of the cavity trailing edge is significantly smaller compared to the spherical dimple. Detailed analyses of different fouling mechanisms (e.g. formation and removal of fouling deposits), including extensive investigations of the interaction between local vortex structures using several vortex identification methods, will be the primary part of the future work.

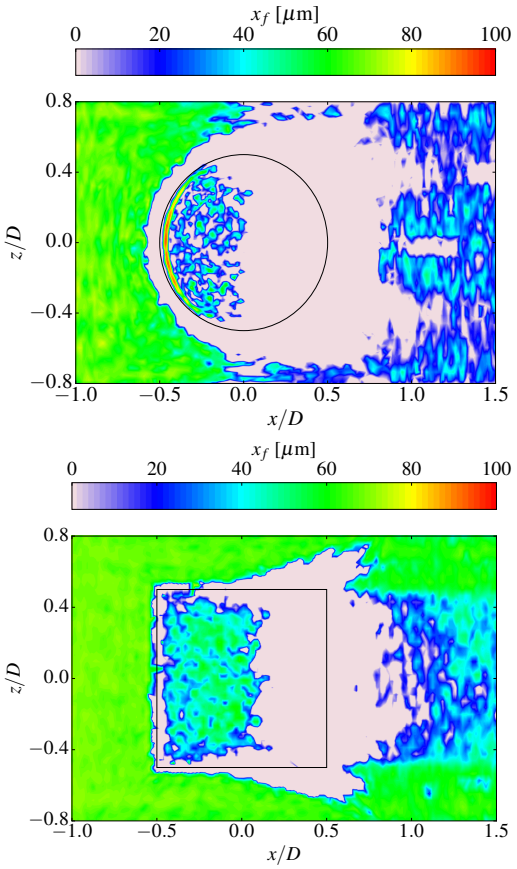

Fig. 6. Distribution and height x_f of the settled fouling layer after 120 s of physical real time for an foulant particle mass loading ratio $\beta = 2 \times 10^{-3}$ at $\mathrm{Re}_D = 42{,}000$: spherical dimple (above), square cavity (below)

CONCLUSIONS

A novel multiphase Eulerian-Lagrangian approach for the numerical simulation of particulate fouling processes of structured heat transfer surfaces is introduced. Time-resolved LES of the turbulent flow inside a smooth channel with a single spherical dimple or square cavity ($t/D = 0.26$, $\mathrm{Re}_D = 42{,}000$) and foulant particle mass loading ratios up to $\beta = 2 \times 10^{-3}$ discloses the following major aspects:

1. Our proposed numerical method is suitable for a physical simulation of particulate fouling processes.
2. The presence of unsteady asymmetric vortex structures inside the spherical dimple could be approved.
3. The spherical dimple shows a 37% higher thermo-hydraulic efficiency in comparison to the square cavity.
4. A considerable lower amount of fouling deposits in the periphery and inside of the spherical dimple due to the distinctive flow structures (improvement of the fouling mitigation ability).

These first results confirm the essential potential of the proposed approach and allows extensive investigations of particulate fouling on structured heat transfer surfaces. Nevertheless, fouling simulations for larger time periods are necessary for a reasonable evaluation of the fouling performance. Notwithstanding the fact that the introduced phase conversion algorithm makes the fouling simulations very efficient, LES with hundred millions of particles (depending on the particle mass loading ratio) are very time consuming. Thus, a procedure for the extrapolation of the fouling layer will be introduced to prevent the enormous computational effort for huge fouling intervals. Additionally, experimental measurements are essential in order to verify and validate our method and will be provided in the near future by the ICTV (Prof. S. Scholl, Dr. W. Augustin) from the TU Braunschweig, Germany.

ACKNOWLEDGMENTS

The authors would like to thank the German Research Foundation (DFG, grant no. KO 3394/10-1 and INST 264/113-1 FUGG) and the North-German Supercomputing Alliance (HLRN) for supporting this work.

NOMENCLATURE

a	thermal diffusivity $(\mathrm{m}^2/\mathrm{s})$
A	area (m^2)
D	diameter (m)
C_A	specific heat capacity $(\mathrm{kJ}/(\mathrm{kg\,K}))$
C_A	added mass coefficient $(-)$
C_D	drag coefficient $(-)$
C_f	Fanning friction factor $(-)$
e	coefficient of restitution $(-)$
f	Darcy friction factor $(-)$
$\mathbf{F}$	force (N)
$\mathbf{g}$	gravitational acceleration $(\mathrm{m}/\mathrm{s}^2)$
h	heat transfer coefficient $(\mathrm{W}/(\mathrm{m\,K}^2))$
$\hbar\varpi$	Lifshitz-Van der Waals energy (eV)
H	channel height (m)
I	moment of inertia $(\mathrm{kg\,m}^2)$
$\mathbf{I}$	unit tensor $(-)$

$\mathbf{J}$	heat flux $(\mathrm{W/m^2})$
k	thermal conductivity $(\mathrm{W/(mK)})$, turbulence kinetic energy $(\mathrm{m^2/s^2})$
K	permeability $(\mathrm{m^2})$
L	length (m)
m	mass (kg)
$\dot{m}$	mass flow $(\mathrm{kg/s})$
p	pressure (Pa)
$\mathbf{S}$	strain rate tensor $(\mathrm{N/m^2})$
t	depth (m), time (s)
T	temperature (K)
V	volume $(\mathrm{m^3})$
x	height (m)
$\mathbf{T}$	torque (Nm)
$\mathbf{u}$	velocity $(\mathrm{m/s})$
$\mathbf{x}$	position (m)
Nu	Nusselt number $(-)$
Pr	Prandtl number $(-)$
Re	Reynolds number $(-)$
α	phase fraction $(-)$
β	mass loading ratio $(-)$
μ	dynamic viscosity (Pas)
ν	kinematic viscosity $(\mathrm{m^2/s})$
ρ	density $(\mathrm{kg/m^3})$
τ	stress $(\mathrm{N/m^2})$

Subscripts/Superscripts

0	smooth channel
b	bulk
c	cell
D	diameter
D_h	hydraulic diameter
f	fluid, fouling
p	particle
rms	root mean square
s	shear
SGS	subgrid-scale
t	turbulent
$\overline{...}$	space-filtered
$\langle ... \rangle$	time-averaged
$\langle \overline{...} \rangle$	space- and time-averaged

REFERENCES

Awad, M. M., 2011, Fouling of Heat Transfer Surfaces, Heat Transfer - Theoretical Analysis, Experimental Investigations and Industrial Systems, InTech.

Bejan, A. and Kraus, A. D., 2003, Heat Transfer Handbook, John Wiley & Sons.

Blöchl, R. and Müller-Steinhagen, H. M., 1990, Influence of Particle Size and Particle/Liquid Combination on Particulate Fouling in Heat Exchangers, Canadian Journal of Chemical Engineering, pp. 585-591.

Crow, T. C., Schwarzkopf, J. D., Sommerfeld, M. and Tsuji, Y., 2011, Multiphase flows with droplets and particles, 2nd ed., CRC Press, Taylor & Francis.

Elghobashi, S., 1994, On predicting particle-laden turbulent flows, Applied Scientific Research, Vol. 52, pp. 309-329.

Elyyan, M. A., Rozati, A. and Tafti, D. K., 2008, Investigation of dimpled fins for heat transfer enhancement in compact heat exchangers, Int. J. Heat Mass Transfer, Vol. 51, pp. 2950-2966.

Epstein, N., 1988, Fouling Science and Technology: Particulate Fouling, NATO ASI Series, Vol. 145, pp. 143-164.

Gee, D. L. and Webb, R. L, 1980, Forced Convection Heat Transfer in Helically Rib-Roughened Tubes, Int. J. of Heat Mass Transfer, Vol. 23, pp. 1127-1136.

Germano, M., Piomelli, U., Moin, P. and Cabot, W. H., 1991, A dynamic subgrid-scale eddy viscosity model, Phys. Fluids, Vol. 3, pp. 1760-1765.

Heinl, E. and Bohnet, M., 2005, Calculation of particle-wall adhesion in horizontal gas-solids flow using CFD, Powder Technol., Vol. 159, pp. 95-104.

Kern, D. Q. and Seaton, R. E., 1969, A Theoretical Ana1ysis of Thermal Surface Fouling, Brit. Chem. Eng., Vol. 4, pp. 258-162.

Kim, W. and Menon, S., 1995, A new dynamic one-equation subgrid-scale model for large eddy simulations, AIAA, Aerospace Sciences Meeting and Exhibit, 33 rd, Reno, NV.

Löffler, F. and Muhr, W., 1972, Die Abscheidung von Feststoffteilchen und Tropfen an Kreiszylindern infolge von Trägheitskräften, Chemie-Ing.-Techn., Vol. 44, pp. 510-514.

Mei, R., 1992, An approximate expression for the shear lift force on a spherical particle at finite Reynolds number, Int. J. Multiphase Flow, Vol. 18, pp. 145-147.

Müller-Steinhagen, H. M., 2010, Fouling of Heat Exchanger Surfaces, VDI Heat Atlas, Springer.

Putnam, A., 1961, Integrable form of droplet drag coefficient, ARS Journal, Vol. 31, pp. 1467-1470.

Saffman, P. G., 1965, The lift on a small sphere in a slow shear flow, J. Fluid Mech., Vol. 22, pp. 385-400.

Saffman, P. G., 1968, Corrigendum to the lift on a small sphere in a slow shear flow, J. Fluid Mech., Vol. 31, pp. 624.

Shah, R. K and Sekulić, D. P., 2003, Fundamentals of Heat Exchanger Design, John Wiley & Sons.

Sommerfeld, M., 2010, Particle Motion in Fluids, VDI Heat Atlas, Springer.

Taborek, J., Aoki, T., Ritter, R.B., Palen, J.W. and Knudsen, J.G., 1972, Predictive Methods for Fouling Behavior, Chem. Eng. Prog., Vol. 68, pp. 69-78.

Talbot, L., Cheng, R. K., Schefer, R. W. and Willis, D. R., 1979, Thermophoresis of particles in a heated boundary layer, J. Fluid Mech., Vol. 101, pp. 737-758.

Terekhov, V. I., Kalinina, S. V. and Mshvidobadse, Y. M., 1997, Heat transfer coefficient and aerodynamic resistance on a surface with a single dimple, Journal of Enhanced Heat Transfer, Vol. 4, pp. 131-145.

Turnow, J., Kornev, N., Isaev, S. and Hassel, E., 2011, Vortex mechanism of heat transfer enhancement in a channel with spherical and oval dimples, Heat Mass Transfer, Vol. 47, pp. 301-313.

Yoshizawa, A. and Horiuti, K., 1985, A statistically-derived subgrid-scale kinetic energy model for the large-eddy simulation of turbulent flows, J. Phys. Soc. Jpn., Vol. 54, pp. 2834-2839.